International Journal of GEOMATE, Nov., 2018 Vol.15, Issue 51, pp.1-8
Geotec., Const. Mat. & Env., DOI: https://doi.org/10.21660/2018.51.86896
ISSN: 2186-2982 (Print), 2186-2990 (Online), Japan

FINITE STRAIN FINITE ELEMENT FORMULATION OF COUPLED SOLID-FLUID MIXTURE FOR DYNAMIC PROBLEMS

*Bhuddarak Charatpangoon[1], Aiko Furukawa[2], Junji Kiyono[3], Shinya Tachibana[4], Tomohide Takeyama[5] and Atsushi Iizuka[6]

[1]Center of Excellence in Natural Disaster Management, Faculty of Engineering, Chiang Mai University, Thailand; [2,3]Graduate School of Engineering, Kyoto University, Japan; [4,5,6]Faculty of Engineering, Kobe University, Japan.

*Corresponding Author, Received: 30 March 2018, Revised: 16 April 2018, Accepted: 14 May 2018

ABSTRACT: Currently, finite element codes for small–strain have been widely applied in geotechnical engineering problems. However, the limitations of these codes are recognized, especially when the strain is large. To overthrow such limitations, finite–strain finite element code for porous media is needed. Therefore, this study aims to implement the finite element code for coupled solid-fluid at finite strain for static and dynamic problems. Firstly, the governing equation for porous media at finite–strain was introduced. Then, the mixed formulation of both phases with respect to the reference coordinates by deriving the governing equations with respect to the reference or current coordinates and by considering the solid and fluid as separate, was given. At present, the code is developed only for elastic regime as its preliminary step. In this study, the proposed code has been verified with the static and dynamic problem. And, the result of the finite–strain finite element code is then compared with the result of the analytical solution and small–strain finite element code within the small–strain regime. Thereafter, the proposed code was used to estimate the response of the earthen dam when subjected to a dynamic load. Finally, the results, discussion, and comparison between small– and finite–strain finite element analyses were presented.

Keywords: Finite element, Finite strain, Porous media, Dynamic, Computation

1. INTRODUCTION

Recently, finite element codes for infinitesimal–strain have been implemented by many researchers [1]. Although these codes are applied widely in both academia and practice, their limitations are recognized, especially when the strain is large. Hence, finite–strain finite element formulations for solids and structures have been developed and implemented by interested groups [2]-[12] developed and implemented finite–strain finite element formulations for porous media.

This study aims to implement a finite–strain finite element code. Firstly, the governing equation for porous media at finite–strain was introduced. Then, the mixed formulation of both phases with respect to the reference coordinates by deriving the governing equations with respect to the reference or current coordinates and by considering the solid and fluid as separate was given. In addition, the verification of the proposed code is necessary. Therefore, the result of the finite–strain finite element code is compared with the result of the analytical solution and small–strain finite element code within the small–strain regime. Then, dynamic analysis of the earthen dam using the proposed code was performed. Finally, the results and comparison between small– and finite–strain finite element analyses were presented.

2. IMPLEMENTATION OF THE NONLINEAR U–P FINITE ELEMENT CODE AT FINITE STRAIN

To develop the finite–strain finite element code, finite continuum mechanics and a governing equation for porous media are developed with the aim of establishing a governing formulation for this problem. Then, the weak form finite element formulation is presented. (For a review, see [3],[13],[14])

2.1 Governing equation

In nonlinear continuum mechanics, the reference configuration and current configuration are of the utmost importance. Any motion defined in space can be assumed to be a continuum within a set of configurations. For each material point X, Lagrangian displacement u(X,t) can be written as below

$$\boldsymbol{u}(\boldsymbol{X},t) = \boldsymbol{x} - \boldsymbol{X} \tag{1}$$

where $\boldsymbol{x}$ and $\boldsymbol{X}$ are the positions of material point $\boldsymbol{X}$ in the current and reference configurations, respectively. The deformation gradient $\boldsymbol{F}$ is the derivative of each component of the deformed $\boldsymbol{x}$ vector with respect to each component of the

reference $\boldsymbol{X}$ vector. The infinitesimal increment of $\boldsymbol{x}$, $d\boldsymbol{x}$ and the deformation gradient $\boldsymbol{F}$ can be written as

$$d\boldsymbol{x} = \boldsymbol{x}\left(\boldsymbol{X} + d\boldsymbol{X}\right) - \boldsymbol{x}\left(\boldsymbol{X}\right), \boldsymbol{F} = \partial\boldsymbol{x}/\partial\boldsymbol{X} \tag{2}$$

Unlike the small–strain, where engineering strain can be applied, the deformation tensors used in finite–strain, are the right and left Cauchy–Green deformation tensors. The right Cauchy–Green deformation tensor $\boldsymbol{C}$ and Green–Lagrangian strain tensor $\boldsymbol{E}$ can be defined as

$$\boldsymbol{C} = \boldsymbol{F}^T\boldsymbol{F}, \boldsymbol{E} = (\boldsymbol{C} - \boldsymbol{I})/2 \tag{3}$$

From this point forward, grad and GRAD represent the gradient operator for the current and reference configuration, respectively. Similarly, div and DIV stand for the divergence operators for the current and reference configuration, respectively. In addition, D( )/Dt and d( )/dt stand for the material time derivative and the total time derivative with respect to the solid phase motion, respectively.

2.2 Balance of Mass

Denote that m_s and m_f are the mass of solid grains and fluid particles, respectively. The mass densities of the solid phase and fluid phase are ρ_s and ρ_f, respectively. φ is a fraction of void space in the material (ratio of the volume of void space to the total volume of material). The total mass of mixture in an arbitrary deformed configuration is given by the volume integrals ($\phi_t(B)$) as

$$m_s = \int_{\phi_t(B)} \rho_s\left(1-\varphi\right)dv \tag{4}$$

$$m_f = \int_{\phi_t(B)} \rho_f\varphi dv \tag{5}$$

By taking the material time derivatives and localizing the results from the argument of arbitrariness, then the following equations for the solid phase and fluid phase were obtained, respectively.

$$\frac{Dm_s}{Dt} = \frac{\partial\left[\rho_s\left(1-\varphi\right)\right]}{\partial t} + div\left[\rho_s\left(1-\varphi\right)\upsilon\right] = 0 \tag{6}$$

$$\frac{Dm_f}{Dt} = \frac{\partial\left(\rho_f\varphi\right)}{\partial t} + div\left(\rho_f\varphi\bar{\upsilon}\right) = 0 \tag{7}$$

where $\bar{v}$ is the intrinsic velocity of the fluid phase. In the fluid phase, the total time derivative of m_f following the solid phase motion is not zero, but instead represents the rate of fluid mass accumulation in the moving volume of the solid phase, and thus

$$\begin{aligned}\frac{Dm_f}{Dt} &= \frac{dm_f}{dt} + \int_{\partial\phi_t(B)} \boldsymbol{q}\cdot\boldsymbol{n}da \\ &= \frac{\partial\left(\rho_f\varphi\right)}{\partial t} + div\left(\rho_f\varphi\boldsymbol{v} + \boldsymbol{q}\right) = 0\end{aligned} \tag{8}$$

where $\boldsymbol{q}$ is the mass flow rate per unit current surface area, and $\boldsymbol{n}$ is the outward unit normal vector to the same surface area. $\partial\phi_t(B)$ denotes surface integrals. The surface flux $\boldsymbol{q}$ is related to the solid and fluid velocities via expression $\boldsymbol{q} = \rho_f\hat{\boldsymbol{v}}, \hat{\boldsymbol{v}} = \varphi\boldsymbol{v}^r$, $\boldsymbol{v}^r = \bar{\boldsymbol{v}} - \boldsymbol{v}$ or $\bar{\boldsymbol{v}} = \boldsymbol{v} + \boldsymbol{v}^r$ where $\boldsymbol{v}^r$ is the relative velocity of the fluid phase to the solid phase, and $\hat{\boldsymbol{v}}$ is the superficial Darcy's velocity. By expanding equations Eq. (6) and Eq. (7), gives

$$-\frac{d\varphi}{\partial t} + \left(1-\varphi\right)\frac{1}{\rho_s}\frac{d\rho_s}{dt} + \left(1-\varphi\right)div\boldsymbol{v} = 0 \tag{9}$$

$$\frac{d\varphi}{\partial t} + \frac{\varphi}{\rho_f}\frac{d\rho_f}{dt} + \varphi\mathrm{div}\boldsymbol{v} + \frac{1}{\rho_f}div\left(\rho_f\hat{\boldsymbol{v}}\right) = 0 \tag{10}$$

for the solid phase and the fluid phase, respectively. Adding the last two equations gives the total mass conservation for the mixture.

$$\begin{aligned}&\mathrm{div}\boldsymbol{v} + \frac{1}{\rho_f}div\left(\rho_f\hat{\boldsymbol{v}}\right) + \left(1-\varphi\right)\frac{1}{\rho_s}\frac{d\rho_s}{dt} \\ &+ \frac{\varphi}{\rho_f}\frac{d\rho_f}{dt} = 0\end{aligned} \tag{11}$$

for the incompressible solid and fluid, Eq. (11) becomes

$$div\boldsymbol{v} + div\hat{\boldsymbol{v}} = 0 \tag{12}$$

2.3 Balance of Momentum

By introducing the Cauchy partial stress tensors for solid $\boldsymbol{\sigma}_s$ and fluid $\boldsymbol{\sigma}_w$, respectively, the Cauchy total stress tensor $\boldsymbol{\sigma}$ is $\boldsymbol{\sigma} = \boldsymbol{\sigma}_s + \boldsymbol{\sigma}_w$. The linear momentum balance equation of the solid phase takes the form

$$\begin{aligned}&\int_{\phi_t(B)} \rho_s\left(1-\varphi\right)\boldsymbol{g}dv + \int_{\phi_t(B)} \boldsymbol{h}_s dv + \int_{\partial\phi_t(B)} \boldsymbol{\sigma}_s\boldsymbol{n}da \\ &= \int_{\phi_t(B)} \rho_s\left(1-\varphi\right)\boldsymbol{a}dv\end{aligned} \tag{13}$$

where $\boldsymbol{g}$ is the vector of gravitational acceleration, $\boldsymbol{h_s}$ is the flow–induced body force arising from the frictional drag of the fluid phase on the solid matrix and $\boldsymbol{a}$ is the material acceleration of the solid phase. Note that the second part of Eq. (13) is

derived by Reynolds transport theorem and balance of solid mass. Thus, Eq. (13) localizes to

$$\rho_s(1-\varphi)\boldsymbol{g}+\boldsymbol{h}_s+div\boldsymbol{\sigma}_s=\rho_s(1-\varphi)\boldsymbol{a} \tag{14}$$

and for the fluid phase, the momentum balance equation can be written as

$$\int_{\phi_t(B)}\rho_f\varphi\boldsymbol{g}dv+\int_{\phi_t(B)}\boldsymbol{h}_f dv+\int_{\partial\phi_t(B)}\boldsymbol{\sigma}_w\boldsymbol{n}da = \frac{\boldsymbol{D}}{\boldsymbol{D}t}\int_{\phi_t(B)}\rho_f\varphi\bar{\mathbf{v}}dv\equiv\int_{\phi_t(B)}\rho_f\varphi\bar{\boldsymbol{a}}dv \tag{15}$$

where $\boldsymbol{h}_f$ is reactive body force exerted by the solid matrix on the fluids and $\bar{\boldsymbol{a}}$ is the material acceleration of the fluid phase. The localization of Eq. (15) can be rewritten as

$$\rho_f\varphi\boldsymbol{g}+\boldsymbol{h}_f+div\boldsymbol{\sigma}_w=\rho_f\varphi\bar{\boldsymbol{a}} \tag{16}$$

Note that $\boldsymbol{h}_s$ and $\boldsymbol{h}_f$ are a pair of internal forces, which naturally will not affect the mixture as a whole. Summation of Eq. (16) and Eq. (14) gives

$$\rho\boldsymbol{g}+div\boldsymbol{\sigma}=\rho_s(1-\varphi)\boldsymbol{a}+\rho_f\varphi\bar{\boldsymbol{a}} = \rho\boldsymbol{a}+\rho_f\varphi\boldsymbol{a}^r,\ \rho=\rho_s(1-\varphi)+\rho_f\varphi \tag{17}$$

where ρ is the total saturated mass density of the solid-fluid mixture, and $\boldsymbol{a}^r=\bar{\boldsymbol{a}}-\boldsymbol{a}$ is the relative material acceleration of the fluid phase relative to the solid phase. Then $\boldsymbol{a}^r\approx 0$ was assumed, and Eq. (17) becomes

$$div\boldsymbol{\sigma}+\rho\boldsymbol{b}=\rho\boldsymbol{a}=\rho\ddot{\boldsymbol{u}} \tag{18}$$

where $\boldsymbol{b}$ is the vector of body force components per unit volume and $\ddot{\boldsymbol{u}}=\boldsymbol{a}$

2.4 Weak Form Finite Element Formulation

To obtain the weak form finite element formulation, the trial solution spaces are introduced using $\boldsymbol{\eta}=\{\boldsymbol{\eta}:\phi(B)|\boldsymbol{\eta}=0\ \ on\,\partial_u\phi(B)\}$ and $\psi=\{\psi:\phi(B)|\psi=0\ \ on\,\partial_h\phi(B)\}$. By introducing trial solution into Eq. (12) and Eq. (18) and integrating over the domain ($\phi(B)$) with respect to the current configuration, the equations becomes

$$\int_{\phi(B)}\boldsymbol{\eta}\cdot div\boldsymbol{\sigma}dv+\int_{\phi(B)}\rho\boldsymbol{\eta}\cdot\boldsymbol{b}dv=\int_{\phi(B)}\rho\boldsymbol{\eta}\cdot\ddot{\boldsymbol{u}}dv \tag{19}$$

$$\int_{\phi(B)}\psi div\mathbf{v}dv+\int_{\phi(B)}\psi div\hat{\mathbf{v}}dv=0 \tag{20}$$

where $\hat{\mathbf{v}}=-\boldsymbol{k}\,gradh$, $\boldsymbol{k}$ is the hydraulic conductivity, and $\boldsymbol{h}$ is the hydraulic head. By introducing the effective stress tensor expression $\sigma_{ij}=\sigma_{ij}^{'}-p_w\delta_{ij}$ into Eq. (19) where $\sigma_{ij}^{'}$ is the effective stress, p_w is pore water pressure and δ_{ij} is the Kronecker delta (δ_{ij} = 1, if i = j, δ_{ij} = 0 otherwise) and integrating by parts on the term $\psi div\hat{\mathbf{v}}dv$ in Eq. (20), gives

$$\boldsymbol{G}(\boldsymbol{u},p_w,\boldsymbol{\eta})= \int_{\phi(B)}\left(grad\boldsymbol{\eta}:\boldsymbol{\sigma}'-div\boldsymbol{\eta}p_w-\rho\boldsymbol{\eta}\cdot(\boldsymbol{b}-\ddot{\boldsymbol{u}})\right)dv - \int_{\partial\phi_{\hat{t}}(B)}\boldsymbol{\eta}\cdot\hat{\boldsymbol{t}}ds=0 \tag{21}$$

$$\boldsymbol{H}(\boldsymbol{u},p_w,\psi)= \int_{\phi(B)}\left(\psi\frac{\dot{J}}{J}-grad\psi\cdot\hat{\mathbf{v}}\right)dv-\int_{\partial_{\hat{q}}\phi(B)}\psi\hat{q}ds=0 \tag{22}$$

where $\hat{\boldsymbol{t}}=\boldsymbol{\sigma n}\ on\ \partial_{\hat{t}}\phi(B)$ (the domain of integration at the boundary of $\hat{\boldsymbol{t}}$) , $\hat{q}=-\hat{\mathbf{v}}\cdot\boldsymbol{n}\ on\ \partial_{\hat{q}}\phi(B)$ (the domain of integration at the boundary of $\hat{q}$), and $\dot{J}=Jdiv\mathbf{v}$.

The alternative forms [15] of the effective stress equation are defined as $\boldsymbol{P}=\boldsymbol{P}^{'}-p_w\boldsymbol{F}^{-T}$, $\boldsymbol{S}=\boldsymbol{S}^{'}-p_w\boldsymbol{C}^{-1}$ where ***P, P'*** and ***S, S'*** refers to the first and second total and effective Piola–Kirchhoff stress tensors, respectively. The relationship among them can be expressed as $\boldsymbol{S}=F^{-1}\cdot\boldsymbol{P}=F^{-1}\cdot\boldsymbol{\sigma}\cdot F^{-T}$; $\boldsymbol{\sigma}$ is the Cauchy–stress tensor. $\boldsymbol{S}$ can be divided into $\boldsymbol{S}_{inv}+\boldsymbol{S}_{vis}$, where $\boldsymbol{S}_{inv}$ and $\boldsymbol{S}_{vis}$ are inviscid and viscous parts of $\boldsymbol{S}$, respectively. For the inviscid part, a compressible Neo–Hookean hyper–elastic material is assumed for the large deformation analysis. The stored energy function of a compressible Neo–Hookean hyperelastic material can be written as [16]

$$\boldsymbol{\Psi}=\frac{\mu}{2}(\boldsymbol{I}_c-3)-\mu\ln J+\frac{\lambda}{2}(\ln J)^2 \tag{23}$$

where λ and μ are the Lame's constants, J is the Jacobian determinant of the deformation gradient $\boldsymbol{F}$, ($J=\det\boldsymbol{F}$) and $\boldsymbol{I}_c$ is the first invariant of the right Cauchy–Green deformation tensor $\boldsymbol{C}$ ($\boldsymbol{I}_c=tr\boldsymbol{C}=\boldsymbol{C}:\boldsymbol{I}$). Thus, the inviscid effective stress can be obtained from

$$\boldsymbol{S}'_{inv}=2\frac{\partial\boldsymbol{\Psi}}{\partial C}=\mu\mathbf{1}+(-\mu'+\lambda'\ln J)\boldsymbol{C}^{-1} \tag{24}$$

where $\boldsymbol{1}$ = (1_{ij} = 1, if i = j, 1_{ij} = 0 otherwise). For the viscous part, we consider a Kelvin solid and postulate the following form

$$\boldsymbol{S}'_{vis}=\alpha\boldsymbol{C}:\left(\tfrac{1}{2}\dot{\boldsymbol{C}}\right) \tag{25}$$

where α is a viscous damping parameter of the solid matrix, and $\boldsymbol{C}$ is the fourth order Lagrangian tangential elasticity tensor which takes the form

$$\boldsymbol{C}=4\frac{\partial^2\boldsymbol{\psi}}{\partial\boldsymbol{C}\partial\boldsymbol{C}}=\lambda'\boldsymbol{C}^{-1}\otimes\boldsymbol{C}^{-1}+2\left(\mu'-\lambda'\ln J\right)\boldsymbol{I}_{C^{-1}} \quad (26)$$

where $\boldsymbol{I}_{(C^{-1})}=\partial(\boldsymbol{C}^{-1})/\boldsymbol{C}$ is rank four tensors with components? Applying a push forward on all four indices of $\boldsymbol{C}$, the Eulerian or spatial elasticity tensor $\boldsymbol{C}$ can be expressed in terms of the effective Lame's constants λ' and μ' as,

$$c_{ijkl}=\lambda'\delta_{ij}\delta_{kl}+2\mu'\left(\frac{\delta_{ik}\delta_{jl}+\delta_{il}\delta_{jk}}{2}\right) \quad (27)$$

where $\lambda'=\lambda/J$ and $\mu'=\left(\mu-\lambda\ln J\right)/J$. Note that in case of small strains where $J = 1$, then, and the standard fourth-order tensor used in the linear elastic analysis is recovered. By taking the derivation with respect to the reference configuration of Eq. (21) and Eq. (22) and substituting constitutive expression, gives

$$\boldsymbol{G}\left(\boldsymbol{u},p_w,\boldsymbol{\eta}\right)=\int_B\left\{\begin{array}{l}\left(\boldsymbol{F}^T\cdot GRAD\boldsymbol{\eta}\right):\boldsymbol{S}'\\-Jp_w\left(GRAD\boldsymbol{\eta}:\boldsymbol{F}^{-1}\right)\\-\rho_0\boldsymbol{\eta}\cdot\left(\boldsymbol{b}-\ddot{\boldsymbol{u}}\right)\end{array}\right\}dV-\int_{\partial_{\hat{t}}B}\boldsymbol{\eta}\cdot\hat{\boldsymbol{T}}dS=0 \quad (28)$$

$$\boldsymbol{H}\left(\boldsymbol{u},p_w,\psi\right)=\int_B\psi\dot{J}dV-\int_B\left\{\left(GRAD\psi\cdot\boldsymbol{F}^{-1}\right)\cdot J\hat{\boldsymbol{v}}_f\right\}dv-\int_{\partial_{\hat{q}}B}\psi\hat{Q}dS=0 \quad (29)$$

where $\rho_0=J\rho$, $\hat{T}$ is $\hat{t}$ with respect to the reference configuration, and $\hat{Q}$ is $\hat{q}$ with respect to the reference configuration, for solid phase and fluid phase, respectively. Please note that B, $\partial_{\hat{t}}B$ and $\partial_{\hat{q}}B$ indicate the integration domain over the volume, and at the boundary of $\hat{t}$ and $\hat{q}$, respectively. By expanding the above equations, the final weak form for solid phase can be written as

$$\begin{aligned}\delta\boldsymbol{G}=&\int_B\left(\boldsymbol{F}^T\cdot GRAD\boldsymbol{\eta}\right):\boldsymbol{C}^{ep}:\left(\boldsymbol{F}^T\cdot GRAD\delta\boldsymbol{u}\right)dV\\&+\int_B GRAD\boldsymbol{\eta}:\left(\boldsymbol{S}'\oplus\boldsymbol{1}\right):GRAD\,\delta\boldsymbol{u}\,dV\\&-\int_B J\,p_w\left(GRAD\,\boldsymbol{\eta}:\boldsymbol{F}^{-T}\right)\left(GRAD\,\delta\boldsymbol{u}:\boldsymbol{F}^{-T}\right)dV\\&-\int_B J\left(GRAD\boldsymbol{\eta}:\boldsymbol{F}^{-T}\right)\delta p_w\,dV\\&+\int_B J\,p_w\left(GRAD\,\boldsymbol{\eta}\cdot\boldsymbol{F}^{-1}\right)^T:\left(GRAD\delta\boldsymbol{u}\cdot\boldsymbol{F}^{-1}\right)dV\\&-\int_B J\,\rho_w\left(GRAD\,\delta\boldsymbol{u}:\boldsymbol{F}^{-T}\right)\boldsymbol{\eta}\\&+\int_B J\rho_w\left(GRAD\delta\boldsymbol{u}:\boldsymbol{F}^{-T}\right)\boldsymbol{\eta}\cdot\ddot{\boldsymbol{u}}dV+\int_B J\rho\boldsymbol{\eta}\cdot\delta\ddot{\boldsymbol{u}}dV\end{aligned} \quad (30)$$

where $\boldsymbol{C}^{ep}$ is the stiffness tensor? And, the final weak form for the fluid phase is

$$\begin{aligned}\delta\boldsymbol{H}=&\int_B\psi\,\dot{J}\left(GRAD\delta\boldsymbol{u}:\boldsymbol{F}^{-T}\right)dV+\int_B\psi\,J\left(GRAD\delta\dot{\boldsymbol{u}}:\boldsymbol{F}^{-T}\right)dV\\&+\int_B\left(GRAD\psi\cdot\boldsymbol{F}^{-1}\right)\cdot\frac{\boldsymbol{k}}{\rho_w g}\cdot\left(GRAD\,\delta p_w\cdot\boldsymbol{F}^{-1}\right)JdV\\&-2\int_B\left(GRAD\psi\cdot\boldsymbol{F}^{-1}\right)\cdot sym\left[\frac{\boldsymbol{k}}{\rho_w g}\cdot\left(GRAD\delta\boldsymbol{u}\cdot\boldsymbol{F}^{-1}\right)^T\right]\cdot\left(GRAD\,p_w\cdot\boldsymbol{F}^{-1}\right)JdV\\&+\int_B\left(GRAD\psi\cdot\boldsymbol{F}^{-1}\right)\cdot\frac{\boldsymbol{k}}{\rho_w g}\cdot\left(GRADp_w\cdot\boldsymbol{F}^{-1}\right)\left(GRAD\delta\boldsymbol{u}:\boldsymbol{F}^{-T}\right)JdV\\&-\int_B\left(GRAD\psi\cdot\boldsymbol{F}^{-1}\right)\cdot\left\{\left(GRADp_w\cdot\boldsymbol{F}^{-1}\right)-\left(GRAD\delta\boldsymbol{u}:\boldsymbol{F}^{-T}\right)\boldsymbol{1}\right\}\cdot\boldsymbol{k}\cdot\frac{\boldsymbol{G}}{g}JdV\end{aligned} \quad (31)$$

where $\boldsymbol{k}$ is the hydraulic conductivity, and $\boldsymbol{G}$ is the elevation head tensor.

Eq. (30) and Eq. (31) can be solved using the Newmark's method with Newton–Raphson iteration [17], [18]. In this study, the constant γ and β are ½ and ¼, respectively.

Convergence criteria based on the norm of the displacements, $\|U\|_2$ and Residuals force, $\|R\|_2$ were used. The norm of those two convergence criteria can be expressed as follow.

$$\|U_2\|=\sqrt{\left(\sum_{i=1}^{n}\left|u_{t+1}-u_t\right|^2\right)}\le\text{TOL} \quad (32)$$

$$\|R_2\|=\sqrt{\left(\sum_{i=1}^{n}\left|R\right|^2\right)}\text{ or }\sqrt{\left(\sum_{i=1}^{n}\left|F_{ext}-F_{int}\right|^2\right)}\le\text{TOL} \quad (33)$$

where u_t and u_{t+1} are displacements at the current step and the next time step, respectively, and F_{ext} and F_{int} are the external and internal forces,

respectively. The tolerances (TOL) were $1x10^{-5}$ and $1x10^{-3}$ for $\|U_2\|$ and $\|R_2\|$, respectively.

3. VERIFICATION

3.1 Static Verification Problem

A numerical example involving the consolidation of a two–dimensional porous media layer was used. The dimension of the numerical model is 1 m × 10 m (80 elements). Fig. 1 describes the boundary condition and flow condition. For static problems, loads of 40 kPa, 2 MPa, 4 MPa, and 8 MPa were applied along the top of the model. Table 1 shows the material properties and the test conditions. A steady-state analytical solution of consolidated vertical displacement for a linear elastic solid phase is $\Delta H = wH / \lambda + 2\mu$ where ΔH is the vertical displacement, λ and μ are the Lame's constants, H is the height of the model, w is the surcharge load, and n_s and n_f are volume fraction of solid phase and fluid phase, respectively. In this study, as the effect of viscous damping is not considered, a viscous damping parameter α is set to be zero.

Table 1 Material properties (Verification)

Parameter	Cases	
	Static	Harmonic
F(MPa)	0.04, 2, 4, 8	1.5(1-cos ω t))
λ(MPa)	29	8.4, 28.85
μ(MPa)	7	5.6, 19.23
k(m/s)	0.1	0.01
ω (rad/s)	NA	50
ρ_s (kg/m^3)	2700	2700
ρ_w (kg/m^3)	1000	1000
n_s	0.58	0.58
n_f	0.42	0.42
H (m)	10	20

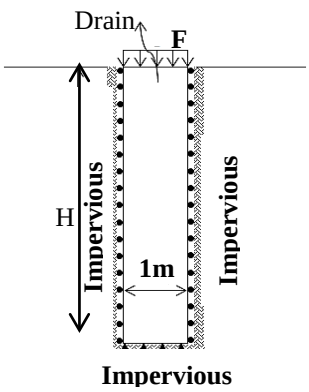

Fig. 1 Numerical model

3.2 Dynamic Verification Problem

The study applied a similar numerical model as in the static verification problem. The dimension of the numerical model is 1 m × 20 m (160 elements). For the dynamic problem, a harmonic load was applied at the top of the mesh as the surcharge load. Table 1 and Fig. 1 show the load function and the model's dimensions and properties. The analytical solution was obtained from previous studies [19], [20].

3.3 Verification Results

Results show that in the static problem when the applied load is 40 kPa (infinitesimal–strain), the results obtained from the finite–strain finite element code show good agreement with the results of both the small–strain finite element code and the analytical solution (Fig. 2). Under larger loads of 2 MPa, 4 MPa, and 8 MPa, the results obtained using the small–strain finite element code approached those of the analytical solution, while the finite–strain finite element code yields a smaller response (Fig. 3). The finite–strain solution is stiffer than the small–strain due to the effect of the addition geometric nonlinear terms in the finite–strain formulation (Table 2).

Table 2 Verification results (Static)

Load (Mpa)	Vertical displacement(m)			% difference
	Analytical	Small-strain	Finite-strain	
0.04	0.0093	0.0093	0.0093	0.0
2	0.4646	0.4646	0.4306	7.3
4	0.9293	0.9293	0.8287	10.8
8	1.8585	1.8585	1.5178	18.3

For the dynamic problem, Fig. 4 and Fig. 5 shows the vertical displacements and the excess pore pressure of the observation points at Z = 0.0 m, 1.0 m, and 2.0 m from the model surface of the finite–strain finite element code, small–strain finite element code, and analytical solution, respectively. It can be summarized that both displacement and excess pore pressure, under a small harmonic load, obtained using the finite–strain finite element code is in a good agreement with the results of both the small–strain finite element code and the analytical solution.

Given that the results of both the static and dynamic problems obtained using the proposed code agree well with the analytical solution and the results of the small–strain finite element code in all aspects, the proposed code can be developed

further to include the advanced constitutive law and applied to the analysis of earth dams or other geotechnical problems.

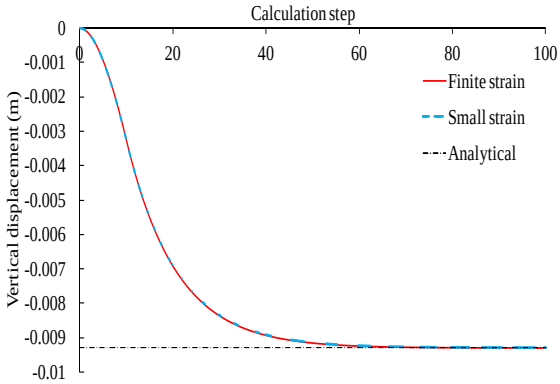

Fig. 2 Verification results of a static problem when applying 40 kPa

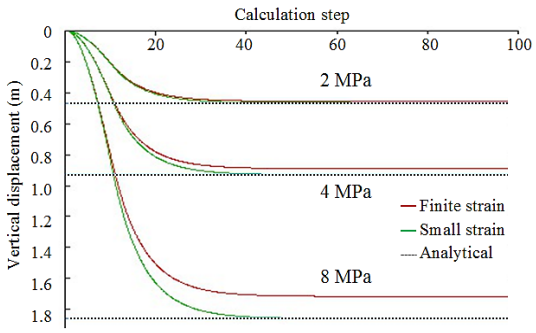

Fig. 3 Verification results of a static problem when applying 2, 4 and 8 MPa

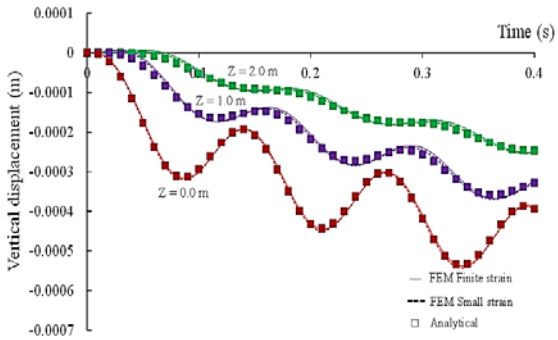

Fig. 4 Vertical displacements

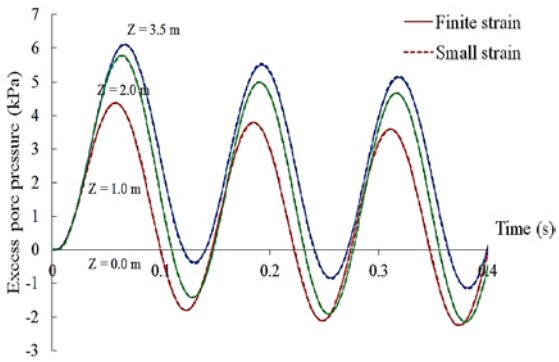

Fig. 5 Excess pore pressure

4. ANALYSIS OF AN EARTH DAM

4.1 Site Description and Input Motion

Fig. 6 shows the typical cross-section of the earthen dam. The embankment dam was an 18.5–m high with a crest width of 6 m. In this study, only the elastic constitutive law is applicable. Table 3 summarizes the material properties of the dam model. Thus, we present analysis and comparison between the results of the small–strain finite element code and the finite–strain finite element code using elastic properties. As a preliminary step, this study used a generated harmonic wave as the input motion, as shown in Fig. 7. The peak ground acceleration, a_{max}, is 3.00 m/s^2 with 15 s shaking duration.

This study proposed rectangular four–node element dam model. Total element number was 456 elements. The foundation was modeled by extending, a 10–m–thick layer, 100 m on either side from the center. The boundary conditions were restrained in the horizontal and vertical directions at the bottom of the model. For both edges, the boundary conditions were fixed only in the lateral direction. For dynamic analysis, the dam was analyzed in undrained condition, neglecting the effect of reservoir pressure and initial stress. All elements were assumed to be in the saturated condition.

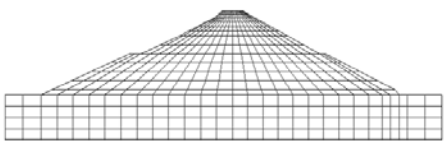

Fig. 6 Dam model

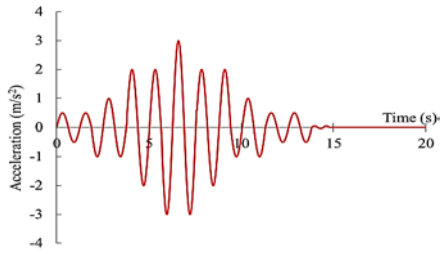

Fig. 7 Input motion

Table 3 Material properties

Properties	Dam body			Base
	Top	Middle	Lower	
γ_{dry} (kN/m^3)	16.0	14.0	16.0	30.0
γ_{sat} (kN/m^3)	18.0	16.0	18.0	-
E (MPa)	50.0	30.0	17.5	300.0
n	0.65	0.44	0.26	-
υ	0.3	0.3	0.3	0.2

4.2 Analysis Results and Discussions

4.2.1 Displacement

The maximum crest's settlement Uy, is 0.00051 m and 0.00041 m for small– and finite–strain, respectively. And, the maximum crest's horizontal displacement, Ux, is 0.0716 m and 0.0715 m (upstream side) for small– and finite–strain, respectively (Fig. 8) (Table 4).

By comparing small–strain and finite–strain finite element codes, it can be seen that for the maximum crest settlement and the maximum horizontal displacement, the small–strain code yielded a value a bit higher than did the finite–strain code. In overall, both codes yield a similar tendency and are in a very good agreement with the differences that are expected due to the different formulations.

4.2.2 Excess pore pressure

The Maximum excess pore pressures were about 36 kPa and 34 kPa for the finite–strain and infinitesimal–strain finite element codes, respectively. Fig. 9 shows the excess pore pressure at 6.62 s. A comparison of small–strain and finite–strain finite element codes shows that, overall, both codes yield a similar tendency and are in very good agreement, with the differences that are expected due to the different formulations.

Table 4 Analysis results

Finite element code	Displacement		Excess Pore pressure (kPa)
	Ux(cm)	Uy(cm)	
Small-strain	7.16	0.051	34.0
Finite-strain	7.15	0.041	36.0

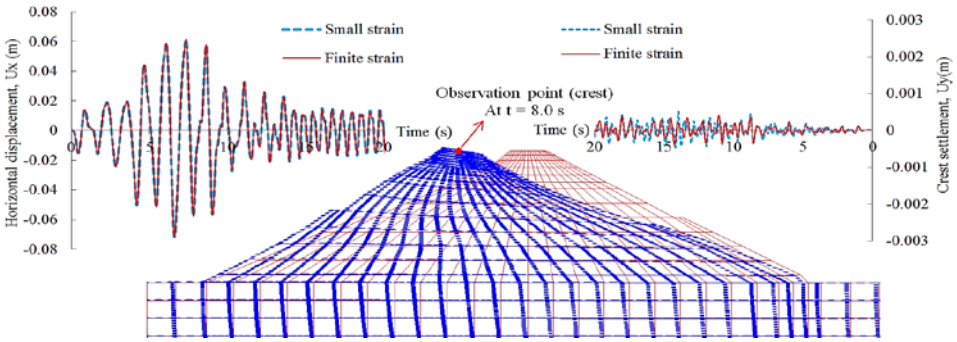

Fig. 8 Displacement

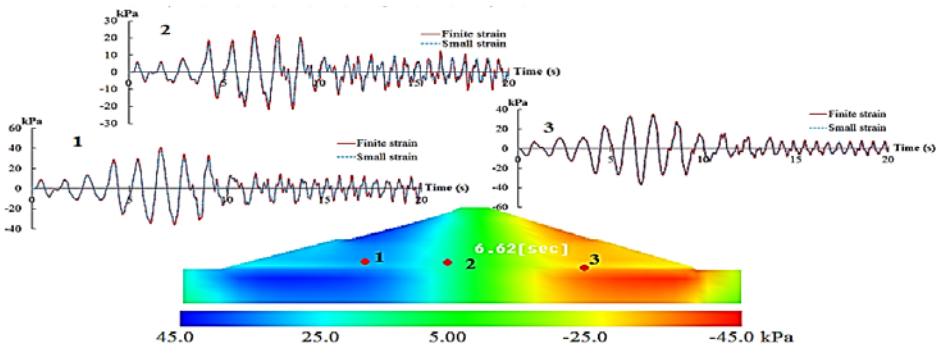

Fig. 9 Excess pore pressure

5. CONCLUSION

The finite–strain finite element code for coupled solid-fluid mixtures under static and dynamic conditions was proposed in this study. The proposed code has been verified using static and dynamic problems. Verification results yield a good agreement in all aspects. The proposed code was used to estimate the response of the earthen dam when subjected to a generated harmonic wave. Comparison of the proposed code and small–strain code indicates that the maximum crest settlement, horizontal displacement, acceleration, and excess pore pressure obtained from the finite–strain finite element code show a similar trend with the values obtained using the small–strain finite element code. The difference between the values obtained using the small–and finite–strain finite element code is expected owing to the effect of the addition geometric nonlinear terms in the finite–strain formulation.

6. REFERENCES

[1] Zienkiewicz, O.C., Chan, A.H.C., Pastor, M., Schrefler, B.A., and Shiomi, T. Computational Geomechanics with Special Reference to Earthquake Engineering, John Wiley and Sons, Chichester, England,1998.

[2] Gabriel, G., and Bathe, K.J., Some Computational Issues in Large Strain Elasto–Plastic Analysis, Computers & Structures, Vol. 56, No. 2/3, 1995, pp. 249–267.

[3] Li, C., Borja, R.I., and Regueiro, R.A., Dynamics of Porous Media at Finite Strain, Computation Methods in Applied Mechanics and Engineering, Vol. 193, 2004, pp. 3837–3870.

[4] Regueiro, R.A., and Ebrahimi, D., Implicit Dynamic Three–dimensional Finite Element Analysis of an Inelastic Biphasic Mixture at Finite Strain Part 1: Application to a Simple Geomaterial, Computer Methods in Applied Mechanics and Engineering, Vol. 199, 2010, pp. 2024–2049.

[5] Uzuoka, R. and Borja, R.I., Dynamics of Unsaturated Poroelastic Solids at Finite Strain, International Journal for Numerical and Analytical Methods in Geomechanics, Vol. 36, 2012, pp. 1535–1573.

[6] Heider, Y., Saturated Porous Media Dynamics with Application to Earthquake Engineering, Yousef Heider's Dissertation Report No II–25, University of Stuttgart, Stuttgart, Germany, 2012.

[7] Karrech A, Poulet T, Regenauer-Lieb K., Poromechanics of Saturated Media Based on the Logarithmic Finite Strain. Mechanics of Materials, Vol.51 (0), 2012, pp. 118–136.

[8] Sun, W. C., Ostien, J. T. and Salinger, A.G., A stabilized Assumed Deformation Gradient Finite Element Formulation for Strongly Coupled Poromechanical Simulations at Finite Strain, International Journal for Numerical and Analytical Methods in Geomechanics. Vol. 37(16), 2013, pp. 2755-2788.

[9] Song, X. and Borja, R.I., Mathematical Framework for Unsaturated Flow in the Finite Deformation Range. International Journal for Numerical Methods in Engineering, Vol. 97(9), 2014, pp.658–682.

[10] Song, X. and Borja, R.I., Finite Deformation and Fluid Flow in Unsaturated Soils with random heterogeneity. Vadose Zone Journal, Vol.13 (5), 2014, pp.1–11.

[11] Sun W, Mota A., A multiscale Overlapped Coupling Formulation for Large-deformation Strain Localization. Computational Mechanics Vol. 54(3), 2014, pp. 803–820.

[12] Vuong, A.T., Yoshihara, L., and Wall, W.A., A General Approach for Modeling Interacting Flow through Porous Media under Finite Deformations, Computer Methods in Applied Mechanics and Engineering,Vol. 283, 2015, pp. 1240-1259.

[13] Lewis, R.W. and Schrefler, B.A., The Finite Element Method in the Static and Dynamic Deformation and Consolidation of Porous Media, John Wiley & Sons Ltd., Baffins Lane, Chichester, United Kingdom, 1998.

[14] Holzapfel, G.A., Nonlinear Solid Mechanics: A Continuum Approach for Engineering, John Wiley & Sons Ltd., Baffins Lane, Chichester, United Kingdom, 2000.

[15] Borja, R.I. and Alarcón, E., A Mathematical Framework for Finite Strain Elastoplastic Consolidation, Part 1: Balance laws, Variational Formulation, and Linearization, Computer Methods in Applied Mechanics and Engineering, Vol. 122, 1995, pp. 145-171.

[16] Bonet, J. and Wood, R.D., Nonlinear Continuum Mechanics for Finite Element Analysis, Cambridge University Press, Cambridge, United Kingdom, 1997.

[17] Bathe, K.J., and Baig, M.M.I., On a Composite Implicit Time Integration Procedure for Nonlinear Dynamics, Computers & Structures, Vol. 83, 2005, pp. 2513–2534.

[18] Chang, S.Y., Studies of Newmark Method for Solving Nonlinear Systems: (i) Basic Analysis, Journal of the Chinese Institute of Engineers, Vol. 27, No. 5, 2004, pp. 651–662.

[19] Simon, B.R., Zlenklewlcz, O.C., and Paul, D.K., An Analytical Solution for the Transient Response of Saturated Porous Elastic Solids, International Journal for Numerical and Analytical Methods in Geomechanics, Vol. 8, 1984, pp. 381–398.

[20] De Boer, R., Ehlers, W., and Liu, Z., One–dimensional Transient Wave Propagation in Fluid–saturated Incompressible Porous Media, Archive of Applied Mechanics, Vol. 63, 1993, pp. 59–72.

Copyright © Int. J. of GEOMATE. All rights reserved, including the making of copies unless permission is obtained from the copyright proprietors.